Editors' Suggestion

Electrically sign-reversible topological Hall effect in a top-gated topological insulator $(Bi,Sb)_2Te_3$ grown on europium iron garnet

J.-F. Wong [1,*] K.-H. M. Chen [1,*] J.-M. Chia,[1] Z.-P. Huang,[2] S.-X. Wang,[1] P.-T. Chen,[1] L. B. Young,[2] Y.-H. G. Lin [2] S.-F. Lee,[3] C.-Y. Mou [1,4] M. Hong [2,†] and J. Kwo [1,‡]

[1]*Department of Physics, National Tsing Hua University, Hsinchu 30013, Taiwan*
[2]*Graduate Institute of Applied Physics and Department of Physics, National Taiwan University, Taipei 10617, Taiwan*
[3]*Institute of Physics, Academia Sinica, Taipei 11529, Taiwan*
[4]*Center for Quantum Science and Technology, National Tsing Hua University, Hsinchu 30013, Taiwan*

(Received 1 September 2023; revised 23 November 2023; accepted 21 December 2023; published 26 January 2024)

The topological Hall effect (THE), an electrical transport signature of systems with chiral spin textures like skyrmions, has been observed recently in topological insulator (TI)-based magnetic heterostructures. The strong spin-orbit coupling and the broken spatial inversion symmetry in such heterostructures could lead to a sizable interfacial Dzyaloshinsky-Moriya interaction, favorable for skyrmion formation and pronounced THE. However, the intriguing interplay between the topological surface state (TSS) and THE is yet to be fully understood. In this work, we report an unprecedentedly large THE signal of ∼10 Ω (∼4 μΩ cm at 2 K) with an electrically reversible sign in a top-gated 4 nm TI $(Bi_{0.3}Sb_{0.7})_2Te_3$ (BST) grown on a ferrimagnetic insulator (FI) europium iron garnet (Eu*IG*). The dependence of THE on temperature, external magnetic field angle, and gate bias was investigated and is consistent with the prediction of a skyrmion-driven THE, amenable to elucidate the origin of THE that occurred in TI-based heterostructures. Moreover, a sign change in THE was discovered as the Fermi level was tuned electrically from the upper (electron-doped region) to the lower parts (hole-doped region) of the gapped BST Dirac cone and *vice versa*. We show that the exploitation of the TSS features has led to a sign-reversal of THE repeatedly in a TI/FI top-gate stack. This discovery may impact technological applications in ultralow power skyrmion-based spintronics.

DOI: 10.1103/PhysRevB.109.024432

I. INTRODUCTION

Three-dimensional topological insulators (TIs), featured with their spin-momentum-locked topological surface states (TSSs) [1,2], have generated enormous interest in spintronics over the past decade. The interplay between the spin-momentum-locked TSS and magnetism results in novel electrical transport phenomena [3]. A well-known example is the observation of quantum anomalous Hall effect (QAHE) in a transition metal-doped TI $(Bi,Sb)_2Te_3$ (BST) [4–6]. Later, much attention was also given to TI-based heterostructures interfaced with magnetic materials (MMs) to attain a long-range magnetic order *via* magnetic proximity effect (MPE). This approach offers notable advantages such as fewer crystal defects causing less spin disorder, more uniformly induced interfacial magnetization, and possibly a higher ferromagnetic Curie temperature (T_C) for a higher temperature QAHE or other spintronic applications [7–15]. In the choice of magnetic layer for proximity-magnetized TI, rare earth iron garnets possess several unique properties, such as high T_C above 500 K, perpendicular magnetic anisotropy (PMA), electrically insulating, and large-area crystalline thin films. The proximity-induced ferromagnetism in TI/rare earth iron garnets with strong PMA has been demonstrated with T_C above 400 K [14,15]. However, most studies of magnetic TI (MTI) were focused on the transport phenomena arising from the nontrivial Berry curvature in reciprocal space. The investigation of the spin textures in real space and their related electrical transport in TI heterostructures remains largely unexplored.

Topological Hall effect (THE), a Hall response that emerges from the deflection of charge carriers flowing through nontrivial chiral spin textures, is a transport signature commonly used to identify these chiral spin textures, such as magnetic skyrmions [16,17]. Apart from the magnetic crystals lacking spatial inversion symmetry (SIS), such as B20-type chiral magnets [18–21], skyrmions have been observed in SIS-broken magnetic heterostructures consisting of materials exhibiting strong spin-orbit coupling (SOC), such as heavy metals (HMs) or TIs [22,23]. The interfacial Dzyaloshinskii-Moriya interaction (DMI) plays a crucial role in stabilizing skyrmions in these SIS-broken magnetic heterostructures [24,25]. In contrast to the high current density required for magnetic domain wall motions (10^{11}–10^{12} A/m^2), the ultralow current density (10^5–10^6 A/m^2) achieved in skyrmion motions brings great prospects in energy-efficient devices for memory and computing technology [17,21,24,26]. THE, being an electrical transport phenomenon, is a promising method of skyrmion detection in the field of skyrmion-electronics [25,27].

*These authors contributed equally to this work
†Authors to whom correspondence should be addressed: mhong@phys.ntu.edu.tw
‡raynien@phys.nthu.edu.tw

 ©2024 American Physical Society

Among many THE studies, there have been debates about the exact origin of the reported Hall responses [28–35]. Because the THE is commonly intertwined with the ordinary Hall effect (OHE) and anomalous Hall effect (AHE), a nonlinear OHE contribution from multicarrier transport or a superposition of multi-AHE contributions could lead to artificial THE features without the actual existence of skyrmions in the system [28–30,32–35]. Consequently, distinguishing the THE signals from other sources becomes crucial. In the former scenario, the angle-dependent Hall measurement is applicable to separate the THE contribution from the multicarrier effect [36]. In the latter scenario of artificial THE generated from multi-AHE contribution, one can conduct two- or three-AHE fits to decompose the signals or conduct minor loop measurements, and ascertain if the Hall responses could indeed result from the overlapping of multi-AHE components [14,31,33,37,38]. Although several reports demonstrated pronounced THE in TI-based heterostructures [31,37,39–44], it is noteworthy that an in-depth discussion on the THE and its correlation to the charge carrier transport of spin-momentum-locked TSS is still lacking. A straightforward way to investigate the relationship between THE and charge carriers in TSS is by implementing an electrical gate bias on TI. So far, the gate-tunable THE has been reported in Mn-doped Bi_2Te_3 films and Cr-doped BST heterostructures [40,43,44]; however, the gate devices were achieved by using $SrTiO_3$ (STO) as a dielectric with a large gate bias of tens of volts [40,43,44], which are unfavorable in practical use. Finding a suitable gate dielectric with excellent carrier tunability and reliability remains a challenging issue and needs to be addressed for both fundamental scientific studies and technological applications.

In this work, we report the observation of THE in TI BST/ferrimagnetic insulator (FI) europium iron garnet (Eu*IG*) bilayers. In particular, we successfully manipulated the amplitude and the sign of THE by altering the carrier density and carrier types using a top electrical gate within a few volts, which has yet to be reported. By adopting a heterostructure of gate oxide/TI/FI, the current flow path and the resulting Hall contribution can be limited to the TI layer, which is rather simple compared to other MTI/TI/MTI or TI/MM heterostructures. Judging from the temperature, magnetic field angle, and gate voltage dependence of Hall measurements, our findings were consistent with a skyrmion-driven THE and less likely to come from a nonlinear OHE caused by the multicarrier transport or a superposition of AHE loops. The largest THE magnitude reached $\sim 10\,\Omega$ ($\sim 4\,\mu\Omega\,\mathrm{cm}$) under an applied gate voltage (V_g) of -0.6 V at 2 K. Most importantly, the pronounced and repeated THE sign reversal occurs when the Fermi level (E_F) is tuned across the gapped Dirac point (DP) of BST, suggesting a unique THE characteristic related to the TSS. Hence, the exploitation of THE in TI-based heterostructures may open a new route in high-density and ultralow-power skyrmion-based devices in spintronics.

II. METHODS

The material growth of BST/Eu*IG* basically followed our previous work [14,45]. In brief, 20-nm-thick FI Eu*IG*(001) films with PMA were grown on GGG(001) by an off-axis magnetron sputtering technique [45]. TI BST films were then deposited on Eu*IG* using molecular beam epitaxy (MBE) with the Bi:Sb composition ratio of 3:7 to reach a bulk insulating TI [14]. Next, for the gate oxide deposition, the samples were transferred from the TI-MBE chamber to a multiple-chamber system containing oxide-MBE and atomic layer deposition (ALD) chambers under ultra-high vacuum (UHV) to avoid contaminations at the TI/oxide interface [46]. A 2-nm-thick e-beam evaporated Y_2O_3 (in the oxide MBE chamber) followed by a 15-nm-thick *in situ* ALD Al_2O_3 was deposited on the pristine BST surface, leading to an unpinned E_F at the interface of gate oxide/BST, based on our extensive expertise of high-κ dielectrics on semiconductor surfaces [47–51]. Finally, the samples were patterned into Hall bars (880 μm × 90 μm) using photolithography and reactive ion etching. To better protect samples for transport measurements, a second Al_2O_3 layer was deposited with a thickness of 25 nm in another *ex situ* ALD system after the fabrication of Hall bars to prevent current leakage from the edges of the Hall bar. All electrical transport measurements were conducted in the physical property measurement system (PPMS). A Keithley 2400 was used to provide a stable voltage source as the gate bias. A Keithley 6221 was used as a current source to generate the alternating current with a root-mean-square amplitude of 100 nA. Two SR830 lock-in amplifiers were used as voltmeters to measure the Hall voltage (V_{yx}) and longitudinal voltage (V_{xx}).

III. RESULTS AND DISCUSSION

A. Physical characterizations of BST/Eu*IG* heterostructures

In this article, we focus on the 4-nm-thick BST thin films grown on Eu*IG*(001), of which the THE-like feature has been repeatedly observed in many samples [14]. The streaky reflection high energy electron diffraction (RHEED) pattern in Fig. 1(a) manifested an atomically ordered, crystalline BST surface with smooth morphology. *Ex situ* atomic force microscopy (AFM) was performed before the photolithography, and the flat BST surface covered by the oxide layers showed a low root-mean-square roughness of 0.633 nm [see Fig. 1(b)].

Figure 1(c) shows the device structure and optical microscope image of the Hall bar. The electrical transport study of BST/Eu*IG* was commenced by measuring longitudinal resistance (R_{xx}) as a function of temperature [see Fig. 1(d)]. R_{xx} increased with decreasing temperatures from 300 to 100 K, revealing a semiconducting behavior caused by the reduction of charge carriers in BST bulk [52,53]. Then, R_{xx} reached a local maximum at $\sim$100 K and decreased as the temperature was further lowered from $\sim$100 to $\sim$10 K, indicating a metallic behavior from the TSS of BST [52,53]. At temperatures below 10 K, R_{xx} increased with decreasing temperatures again, which could be attributed to the electron-electron interaction (EEI) [54]. The longitudinal conductance (G_{xx}) was proportional to the natural logarithm of T, as shown in the inset of Fig. 1(d), consistent with the two-dimensional EEI of the TSS [55,56].

The R_{xx} and Hall resistance (R_{yx}) as a function of magnetic field (H) are presented in Figs. 1(e) and 1(f), respectively. The R_{xx} (R_{yx}) was symmetrized (antisymmetrized) as a

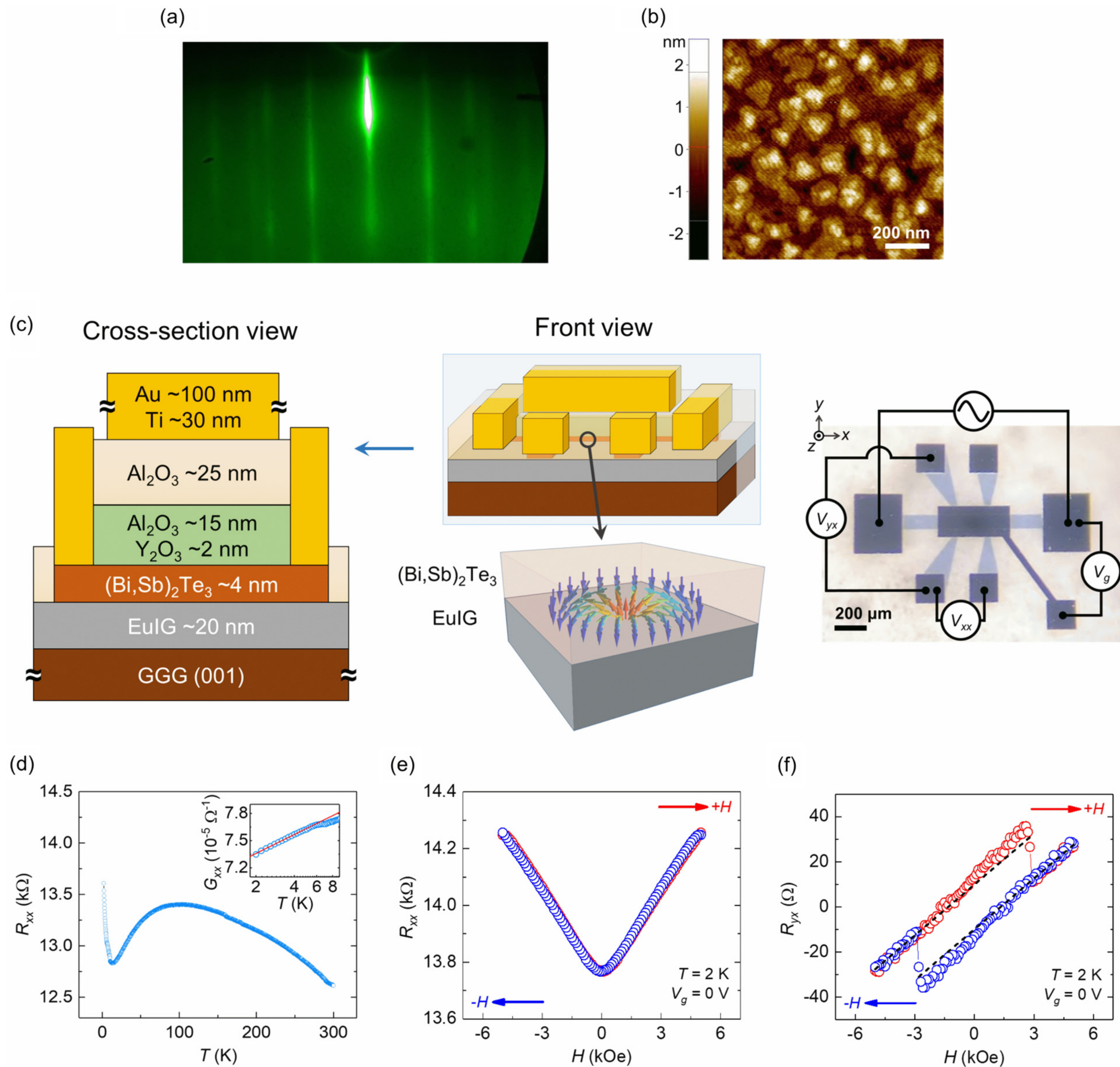

FIG. 1. Sample characterization and schematic illustration of a top-gated BST/Eu*IG* device. (a) RHEED pattern of the 4 nm BST(001) surface along the [100] axis. (b) Surface morphology of 15 nm ALD-Al_2O_3/2 nm e-beam evaporated-Y_2O_3/4 nm MBE-BST/20 nm sputtering-Eu*IG*/GGG(001) in a 1×1 μm^2 area by using AFM. (c) Schematics of a cross-section view and a front view of our top-gated BST grown on Eu*IG*, in which a light blue vertical plane is to dissect the sample structure for the cross-section view. Also shown are the Néel-type skyrmion spin texture at the BST/Eu*IG* interface, and the optical microscope image of a Hall bar device with our measurement setup. (d) R_{xx} as a function of temperature. The inset in (d) shows the G_{xx} as a function of temperature and the fit with a logarithmic function of T. (e) R_{xx} and (f) R_{yx} as a function of magnetic field with an applied V_g of 0 V at 2 K. The dashed lines in (f) represent the extrapolation of the linear OHE background above the H_c.

function of magnetic fields to eliminate the possible R_{yx} (R_{xx}) component resulting from some slight electrode misalignment; a detailed description of the data processing is given in Sec. I of the Supplemental Material [57] (see also Refs. [14,16,31,32,37,39,70–73] therein). At zero fields, a pronounced dip feature was observed in R_{xx}, indicating the presence of the weak antilocalization (WAL) effect [see Fig. 1(e)]. Because of the MPE, a suppressed WAL was observed, as expected in BST/Eu*IG*, which came from the weak localization of the bottom TSS interfaced with Eu*IG* [14]; detailed discussion on the WAL behavior is given in Sec. II of the Supplemental Material [57] (see also Refs. [12,14,74–79] therein). On the other hand, deviation of R_{yx} from the linear background was observed in the H from −1.5 to 3 kOe in the up-sweep (red) curve and −3 to 1.5 kOe in the down-sweep (blue) curve. [see Fig. 1(f)] As discovered in the previous literature, the existence of the TSS in TI-based magnetic heterostructures could generate a strong interfacial DMI, giving rise to topological magnetic structures with a pronounced THE [31,37]. We thus analyzed the Hall data considering three contributions, OHE, AHE, and THE.

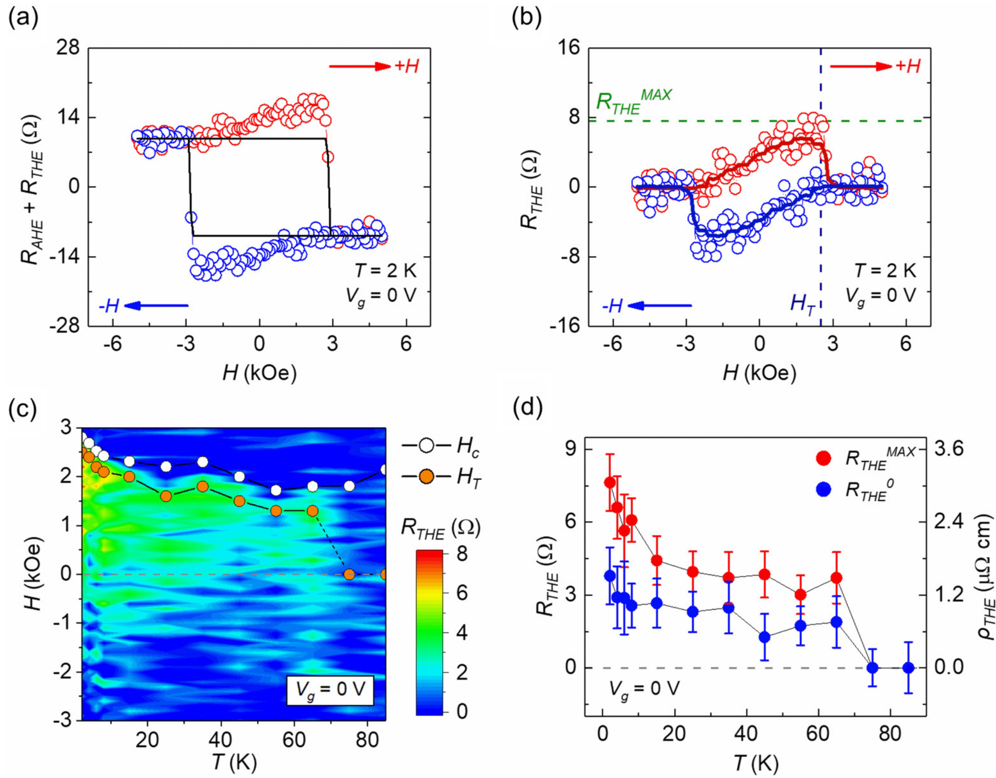

FIG. 2. Temperature-dependent THE properties of BST/Eu*IG*. (a) Coexistence of AHE and THE with an applied V_g of 0 V at 2 K. The scattered points are the Hall data after subtracting a linear OHE background, and the solid line is the fitted AHE contribution. (b) The THE at $V_g = 0$ V; the scattered points are the R_{THE} data, and the lines are guides to the eye. (c) Temperature dependence of H_c and H_T, and a color map of R_{THE} as a function of temperature and magnetic field with an applied V_g of 0 V; the H field was swept from negative to positive. (d) The temperature dependence of $R_{\mathrm{THE}}{}^{\mathrm{MAX}}$ and $R_{\mathrm{THE}}{}^{0}$.

B. Extraction of the topological Hall resistance from the Hall measurements

The OHE contribution is mostly regarded as a linear background in the Hall measurements [31,37,39–42], which is also the assumption used in this work. Knowing that a nonlinear OHE may exist at low fields because of the multicarrier transport [58–60], we performed additional data analysis and examined the possibility of nonlinear OHE background from four different aspects, angle-dependent Hall data in Sec. III D, comparison to other thicknesses of BST grown on Eu*IG*/GGG, curve fittings using a bicarrier model for 4-nm BST/Eu*IG*/GGG, and conducting control experiments on 4 nm BST/GGG in Sec. III of the Supplemental Material [57] (see also Refs. [14,58–60] therein). Moreover, since the magnetic layer Eu*IG* is insulating, the measured Hall contribution entirely came from BST. Given that the E_F of BST was very close to the charge neutrality point (CNP), the charge carriers mainly stemmed from the TSS. Although we cannot preclude the multicarrier transport in our BST films, the nonlinearity of OHE contribution at low fields is minor compared to the excessive Hall signals in the Hall measurements; thus, the OHE contribution is considered as a linear term in the Hall data processing.

Figure 2(a) displays the Hall resistance of the ungated 4 nm BST/Eu*IG* at 2 K after the subtraction of the linear OHE background. In addition to the MPE-induced AHE loop following the square-shaped magnetic hysteresis of Eu*IG* [14,45], excessive Hall signals were observed over a wide range of magnetic fields within the coercive field (H_c). These excessive Hall signals reached the largest value near the H_c and behaved like THE. We subsequently performed two additional experimental checks, the minor loop approach and AHE curve fittings, to resolve the issue of artificial THE composed of two AHE contributions. In the former method, the Hall traces coincided under successively increasing sweeping magnetic fields as the expected behavior of THE responses with only one AHE loop [33]. (see Sec. IV of the Supplemental Material [57] and also Refs. [28–30,32–34] therein) In the latter method, although the Hall signals could be well fitted with two AHE contributions mathematically, it is rather difficult to reconcile their dependence on temperatures as well as gate biases with a reasonable or existing physical picture. (see Sec. V of the Supplemental Material [57]) Therefore, considering the strong SOC provided by TI BST and the broken SIS at the interface between BST and Eu*IG*, it is highly possible that the interfacial DMI helps stabilize the chiral spin texture at the interface between BST and Eu*IG*; these excessive Hall signals are very likely to result from a genuine THE.

The THE resistance (R_{THE}) was further extracted by subtracting the AHE resistance (R_{AHE}). In view of the square magnetic hysteresis observed in the alternating gradient magnetometer measurement of BST/Eu*IG* at 300 K, and square

MPE-induced AHE loops at temperatures without the existence of THE, we here fit the AHE component using $R_{\mathrm{AHE}} = R_{\mathrm{AHE}}{}^{\mathrm{MAX}} \tanh(\frac{H \pm H_c}{H_0})$, where $R_{\mathrm{AHE}}{}^{\mathrm{MAX}}$ and H_0 are the maximum of the R_{AHE} and fitting parameter, respectively [31,37]. Detailed discussion on this data processing is given in Sec. VI of the Supplemental Material [57] (see also Refs. [14,45] therein). After the subtraction of the square AHE loop [black solid line in Fig. 2(a)], the R_{THE} data is shown in Fig. 2(b). THE occurs in both positive and negative fields within the H_c. In this region, the magnetic moments transit from up to down states or down to up states, which can favor the formation of chiral spin textures. The maximum of the R_{THE} is denoted by $R_{\mathrm{THE}}{}^{\mathrm{MAX}}$, and the H field corresponding to the $R_{\mathrm{THE}}{}^{\mathrm{MAX}}$ is denoted by H_T. A giant $R_{\mathrm{THE}}{}^{\mathrm{MAX}}$ of $\sim$8 Ω was observed without an applied V_g at 2 K. At the applied V_g of -0.6 V, the $R_{\mathrm{THE}}{}^{\mathrm{MAX}}$ reached the largest value of $\sim$10 Ω ($\sim$4 $\mu\Omega$ cm). The THE magnitude in this work is the second largest among the reported TI-based bilayer systems [31,37,39,41,42]. (see Table S1 of the Supplemental Material [57] and also Refs. [31,36,37,39,41,42,66,67] therein)

C. Temperature dependence of the topological Hall effect

Next, we discuss the temperature dependence of THE in BST/Eu*IG*. As presented in Figs. 2(c), 2(d), and S10 of Supplemental Material [57], the THE gradually diminished with increasing temperatures and disappeared at 75 K, which could be attributed to the thermal fluctuation or the reduced DMI strength, consistent with the previous studies in TI-based systems [14,31,37,39–41,43]. Furthermore, shown in the color map of Fig. 2(c) is the temperature dependence of H_T that follows closely with that of H_c. This observation is in accord with reports on the THE driven by the magnetization reversal process in systems hosting magnetic skyrmions [37,61]. It is noteworthy that our THE was also found at zero fields, suggesting a robust skyrmion phase without the support of an external magnetic field, similar to the observation in FeGe [62,63]. The R_{THE} at zero fields ($R_{\mathrm{THE}}{}^{0}$) showed an akin temperature dependence to that of $R_{\mathrm{THE}}{}^{\mathrm{MAX}}$ and also vanished at 75 K, as demonstrated in Fig. 2(d). Unlike other B20 compounds, such as FeGe or MnSi, which could exhibit complicated magnetic phases, the magnetic phase diagram can be much simpler in heterostructures made of TI/FI or HM/FI, simplifying the contributions to the Hall signals [31,64–66]. Another difference we notice is that THE can be observed at a high temperature in HM/FI, but THE in TI-based heterostructures emerges mostly at low temperatures. At low temperatures, MPE became a dominant source for inducing the AHE, suggesting that the magnetized bottom TSS may also play an important role besides the strong SOC in TI and broken SIS at the interface. Compared with other TI-based heterostructures, the critical temperature for observing the THE in this work is notably higher than those reported in Cr-doped BST/BST (18 K) [39], Cr_2Te_3/Bi_2Te_3 (20 K) [42], and BST/MnTe (20 K) [41], but slightly lower than $Bi_2Se_3/BaFe_{12}O_{19}$ (80 K) and $CrTe_2/Bi_2Te_3$ (100 K) [31,37]. (see Table S1 of the Supplemental Material [57] and also Refs. [31,36,37,39,41,42,66,67] therein)

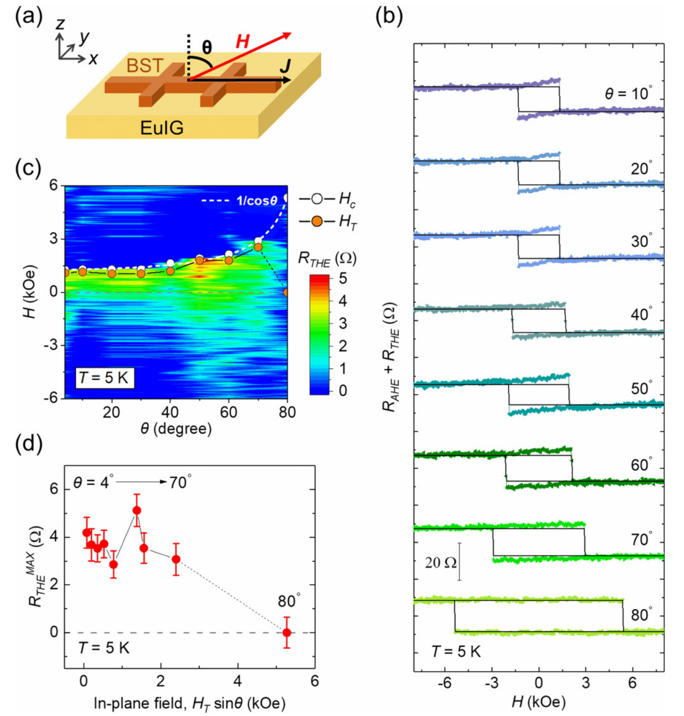

FIG. 3. Angular dependence of THE from 10° to 80° at 5 K of BST/Eu*IG*. (a) A schematic of the angle-dependent Hall measurements. (b) Angular dependence of the AHE loops plus the THE. (c) Magnetic field angle dependence of H_c and H_T, and a color map of R_{THE} as a function of magnetic field angle and H field; the H field was swept from negative to positive. The white dashed line in (c) is the fitted curve of H_c as a function of $1/\cos\theta$. (d) $R_{\mathrm{THE}}{}^{\mathrm{MAX}}$ as a function of *in-plane* magnetic field ($H_T \sin\theta$).

D. Angular dependence of the topological Hall effect

To deepen our understanding of the THE in BST/Eu*IG*, we further investigated the angular dependence of the Hall effect data with the measurement geometry illustrated in Fig. 3(a). The angle θ is defined as the angle between the external magnetic field H and the surface normal direction $+z$ in the x-z plane. The Hall traces at 5 K after subtracting the linear OHE background from 10° to 80° are demonstrated in Fig. 3(b). The AHE loops expanded with increasing θ. The H_c enlarged and was proportional to $1/\cos\theta$ [white dashed line in Fig. 3(c)], indicating that a larger external magnetic field was needed to flip the magnetization in BST to the opposite direction as the θ increased. The R_{THE} data is further plotted as a function of θ and H field, as shown in the color map of Fig. 3(c); the H field was swept from negative to positive. Similar to the temperature dependence of H_T and H_c discussed in the previous paragraph, the angular dependence of H_T also followed closely with that of H_c before the disappearance of THE.

To better elucidate the angle-dependent results, the magnitude of THE was discussed as a function of the *in-plane* component of the applied magnetic field. Because the H_T closely followed the trend of H_c before the disappearance of THE, the H_T was approximately proportional to $1/\cos\theta$,

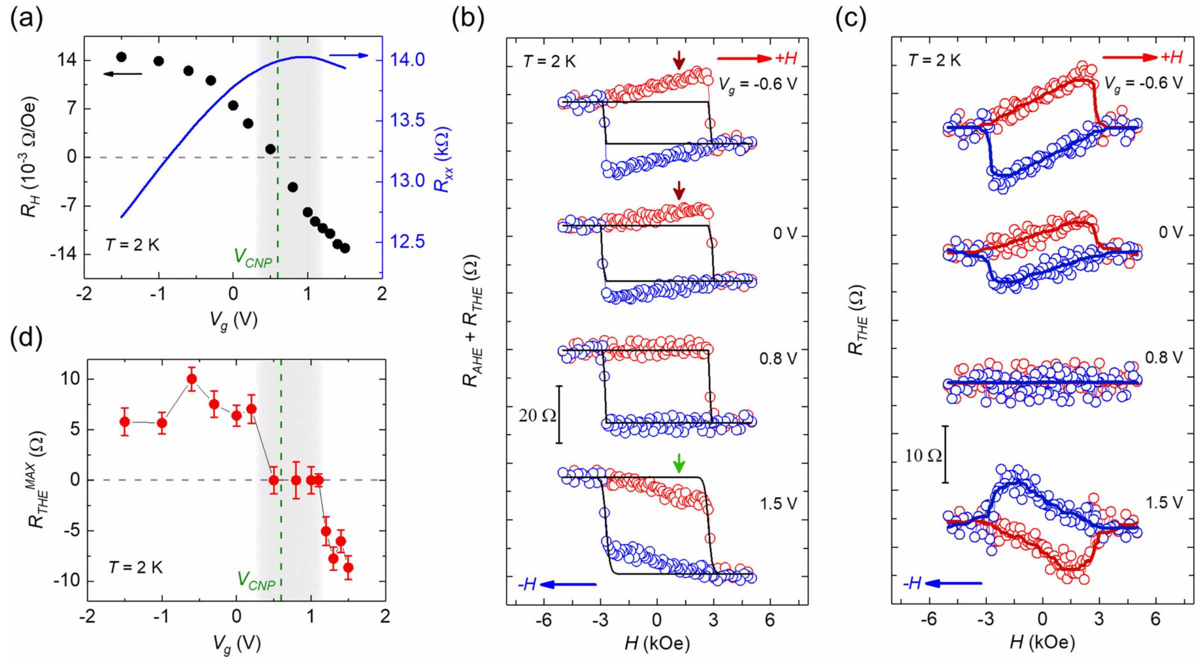

FIG. 4. Gate-bias dependence of THE from −1.5 V to 1.5 V at 2 K of BST/Eu*IG*. (a) Top-gate voltage dependence of R_H (left) and R_{xx} (right). Small R_H and large R_{xx} occurred in the vicinity of CNP (the gray-shaded region). (b) Concurrence of AHE and THE with selected gate voltages. The dark red and green arrows in (b) indicate the hump and dip features near the H_c, respectively. (c) THE with selected gate voltages; the scattered points are the R_{THE} data, and the lines are guides to the eye. (d) Top-gate voltage dependence of $R_{\text{THE}}{}^{\text{MAX}}$ at 2 K. THE disappeared in the vicinity of CNP (the gray-shaded region).

indicating that the *out-of-plane* component of the applied field (H cosθ) was nearly the same when the $R_{\text{THE}}{}^{\text{MAX}}$ occurred. Therefore, we plotted the $R_{\text{THE}}{}^{\text{MAX}}$ as a function of the *in-plane* magnetic field H_T sinθ, as shown in Fig. 3(d). To give a reasonable estimate of the critical field for the disappearance of THE, H_c sin80° was used for the data point of $\theta = 80°$. Judging from Fig. 3(d), the $R_{\text{THE}}{}^{\text{MAX}}$ remained nearly the same with a moderate *in-plane* magnetic field (0.1–2.4 kOe), as attributed to the robustness of the topologically protected skyrmions and similar to the work of Peng *et al.* [31]. The critical *in-plane* field for the disappearance of THE was between 2.4–5.3 kOe. The vanished THE above 5.3 kOe suggests the collapse of the skyrmionic state [36,66–68]. Similar angular behavior of THE was reported in the $\text{Mn}_{1-x}\text{Fe}_x\text{Si}$, a well-known B20-type chiral magnet hosting magnetic skyrmions, with the disappearance of THE at 55° [36]. (see Table S1 of the Supplemental Material for the comparisons with other materials [57] and also Refs. [31,36,37,39,41,42,66,67] therein) This observation of critical angle θ or in-plane field yields that the additional Hall resistance besides the square AHE loop is less likely attributed to the multicarrier effect. Suppose that the nonlinear OHE contribution results in the THE-like feature in this work; this artificial THE-like feature should persist at 80° or even higher angles. Hence, our observation of angle-dependent results in THE supports the existence of skyrmions at the BST/Eu*IG* interface as well.

E. Topological Hall effect and its relationship to the Fermi level

In the following paragraph, we demonstrate the manipulation of THE by implementing a top electrical gate bias on BST. Figure 4(a) shows the gate dependence of R_{xx} and ordinary Hall coefficient (R_H) derived from the slope of the linear OHE background. The E_F was successfully tuned across the gapped DP of BST *via* the gate bias, as manifested by reaching a maximum in R_{xx} and the sign change of R_H near the CNP [the gray-shaded region in Fig. 4(a)]. The CNP here is expected to be located at the center of the MPE-induced gap of TSS in BST. Moreover, the small applied V_g for the CNP (V_{CNP}) of ∼0.6 V indicated that the E_F of our ungated BST was close to the center of the magnetic gap, providing an excellent starting point to alter the carrier type and the carrier density of BST, thus to explore the THE behavior under an external electric field.

Figure 4(b) displays the gate dependence of selected AHE loops together with THE; the scattered points are the measured $R_{\text{AHE}} + R_{\text{THE}}$ data, and the solid lines are the fitted AHE contributions. In the p-type region ($V_g < V_{\text{CNP}}$), a *hump* was found near the H_c as the H field was swept from negative to positive. [dark red arrows in Fig. 4(b)] In the n-type region ($V_g > V_{\text{CNP}}$), a *dip* was observed instead near the H_c [a green arrow in Fig. 4(b)]. With the applied $V_g \sim V_{\text{CNP}}$, the measured data became a square hysteresis loop, a typical feature of AHE without excessive Hall signals from THE. To extract the magnitude of THE, we subtracted the AHE contributions (black solid lines) and plotted R_{THE} in Fig. 4(c). Positive THE was identified in the p-type region of the up-sweep (red) curves, while negative THE was observed in the n-type region. More data of gate-dependent THE loops with finer voltage steps are presented in Fig. S11 of the Supplemental Material [57]. The gate bias dependence of $R_{\text{THE}}{}^{\text{MAX}}$ is further summarized in Fig. 4(d).

To gain a better insight into the mechanism responsible for the sign reversal in THE, we examined R_{THE} and its

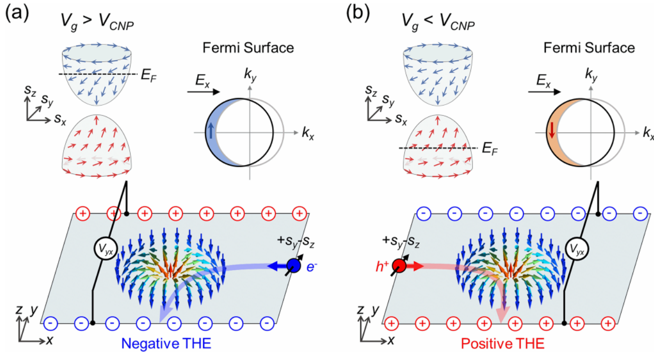

FIG. 5. Illustration of the sign reversal in THE with varying gate bias. Schematics for gapped TSS, the Fermi surface with the application of current in $+x$ direction, and the corresponding THE with (a) $V_g > V_{\text{CNP}}$ (n-type region, E_F located at upper gapped TSS) and (b) $V_g < V_{\text{CNP}}$ (p-type region, E_F located at lower gapped TSS), respectively.

relations to other physical quantities. When a charge carrier flows through magnetic skyrmions, it will experience an effective electromagnetic field $B_{\text{eff}} = n_{sk}\ \Phi_0$, where n_{sk} is the skyrmion density and Φ_0 is the magnetic flux quantum [16]. The resulting Hall resistance is commonly approximated as

$$R_{\text{THE}} \approx R_H P\, n_{sk} \Phi_0, \tag{1}$$

where P is the local spin polarization of the conduction carrier following the spin texture of the skyrmion [16,37]. When the E_F is tuned from the upper Dirac cone to the lower Dirac cone, the majority charge carriers will be altered from electrons to holes, leading to a sign change in R_H. In the meantime, the electron spin polarization is flipped to the opposite direction because of the spin-momentum locking of the gapped TSS (see the Fermi surface in Fig. 5). Since the propagation direction of holes is opposite with respect to that of electrons, the spin orientation for electrons and holes will thus be the same [69], giving rise to the unchanged sign of the exchange coupling between charge carrier spins and local spin texture of skyrmion, i.e., the same sign of P. Therefore, the sign of THE will be switched from negative to positive when the E_F is varied from the upper to the lower parts of the Dirac cone, as illustrated in Fig. 5. The E_F modulation by the gate bias in Fig. 4 was estimated roughly to be from ∼84 meV ($V_g = +1.5$ V) above the gapped DP to ∼128 meV ($V_g = -1.5$ V) below the gapped DP, as detailed in Sec. X of the Supplemental Material [57] (see also Ref. [80] therein).

In the vicinity of CNP, namely $R_H \to 0$, the vanishing R_{THE} could be attributed to the nearly equal numbers of n- and p-type charge carriers. The absence of the THE signals with the E_F near the CNP was also observed in the Cr-doped BST sandwich heterostructures [43,44]. However, in their reports, R_{THE} did not show a sign reversal with the applied gate voltages; the majority carrier type remained the same in both $V_g < V_{\text{CNP}}$ and $V_g > V_{\text{CNP}}$ regions, as suggested from the slopes of their Hall traces. In contrast, this work demonstrated an effective manipulation of charge carriers and THE *via* a top electrical gate. Moreover, our gate bias-dependent results lent strong support to a skyrmion-driven THE in the BST/Eu*IG* heterostructure, which can be well described by Eq. (1) for both positive and negative biases. The same behavior of THE manipulation *via* the top-gate bias was confirmed in another sample (see Fig. S12 of the Supplemental Material [57]). In addition, the difference between the current work and the previous work of Zou *et al.* was clarified and highlighted in Sec. XII of the Supplemental Material [14,57]; the results are consistent among these two samples. Given these findings, inspecting the sign change in THE by tuning the E_F across the CNP could be another viable way to differentiate the genuine and artificial THE in TI-based heterostructures. The electrically sign-reversible THE in TI/FI heterostructures could be a unique feature directly associated with the gapped TSS. This phenomenon has not been observed and might well be absent in other non-TI skyrmion systems, such as chiral magnets or HM/FI heterostructures like Pt/TmIG.

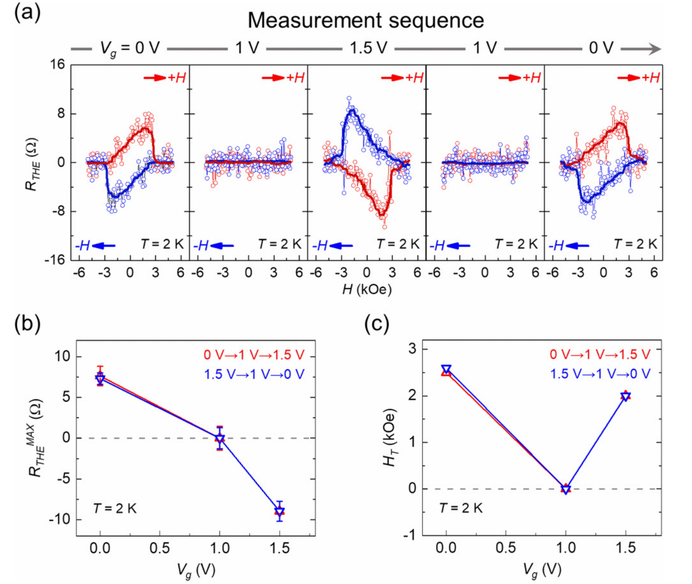

FIG. 6. Repeated switching of THE in BST/Eu*IG*. (a) THE loops with applied V_g in the sequence of 0, 1, 1.5, 1, and 0 V; the scattered points are the R_{THE} data, and the lines are guides to the eye. The corresponding modulation of (b) $R_{\text{THE}}{}^{\text{MAX}}$ and (c) H_T as a function of V_g.

F. Repeated switching of the topological Hall effect with an electric field

Finally, to further examine the reliability of the field-effect device and the reproducibility of the sign reversal in THE, we performed the THE measurements with a series of selected gate biases. As displayed in Fig. 6(a), the THE was reversibly switched. The $R_{\text{THE}}{}^{\text{MAX}}$ and H_T values remained nearly identical to the starting ones, as demonstrated in Figs. 6(b) and 6(c). Although the repeated switching of this "THE" device is currently limited by the robustness of our gate oxides after applying excessive gate bias, the achievement of THE switching within only a few volts demonstrates tremendous progress in manipulating this phenomenon. The idea of an electrically tunable THE field-effect device may open up a new avenue in skyrmion-based spintronic applications.

IV. CONCLUSION

In summary, we have demonstrated the electrically sign-reversible THE in a top-gated TI BST on a FI Eu*IG*. The magnetotransport behaviors on temperature, external magnetic field angle, and gate bias were consistent with a skyrmion-driven THE and less likely to result from alternative mechanisms of nonlinear OHE contribution or superimposed AHE loops. Moreover, the sign change in THE *via* an electrical gate could be a distinctive feature related to the gapped TSS in TI/FI compared to other non-TI skyrmion systems, such as chiral magnets and HM/FI heterostructures. Our findings are thus viable for an in-depth understanding of THE in a TI-based heterostructure. The BST/Eu*IG* bilayer could serve as an excellent platform for studying the interplay among magnetism, chiral spin textures, and topological band structures. Especially, the reproducible electrical manipulation of THE within a few volts may be promising for ultralow-power skyrmion-related applications. Further investigations on direct imaging of skyrmion spin structures in real space will be essential, and experiments *via* scanning microscopy methods, such as spin-polarized scanning tunneling microscopy and scanning transmission x-ray microscopy, are now underway.

ACKNOWLEDGMENTS

The authors thank Prof. H.-H. Lin, Prof. T. R. Chang, K.-Y. Lin, W.-N. Chen, W.-J. Zou, and H.-N. Chen for helpful discussions. This work was financially supported by the National Science and Technology Council (NSTC) of Taiwan under Grants No. NSTC 111–2112-M-007–043 and NSTC 111–2622–8–002–001, and the Center for Quantum Science and Technology and Department of Physics, National Tsing Hua University, Hsinchu 30013, Taiwan (Grant No. NSTC 111–2634-F-007–006). The authors acknowledge resources and support from the Quantum Materials Shared Facilities of Institute of Physics, Academia Sinica. The authors also thank the technical support from Taiwan Semiconductor Research Institute (TSRI), Taiwan.

J.-F.W. and J.-M.C. fabricated the Hall bar device, and collected and analyzed the transport data. Z.-P.H., S.-X.W., and P.-Z.C. produced the BST/Eu*IG* samples. S.-X.W. conducted the magnetic measurements. L.B.Y. and Y.-H.G.L. deposited the *in-situ* top gate oxides. S.-F.L. and C.-Y.M. provided scientific inputs. J.K. and M.H. supervised the project. J.-F.W., K.-H.M.C., and J.K. composed and wrote the manuscript with the comments of all the authors.

[1] X.-L. Qi, T. L. Hughes, and S.-C. Zhang, Phys. Rev. B **78**, 195424 (2008).
[2] M. Z. Hasan and C. L. Kane, Rev. Mod. Phys. **82**, 3045 (2010).
[3] Y. Tokura, K. Yasuda, and A. Tsukazaki, Nat. Rev. Phys. **1**, 126 (2019).
[4] C.-Z. Chang, J. Zhang, X. Feng, J. Shen, Z. Zhang, M. Guo, K. Li, Y. Ou, P. Wei, L.-L. Wang *et al.*, Science **340**, 167 (2013).
[5] J. G. Checkelsky, R. Yoshimi, A. Tsukazaki, K. S. Takahashi, Y. Kozuka, J. Falson, M. Kawasaki, and Y. Tokura, Nat. Phys. **10**, 731 (2014).
[6] X. Kou, S.-T. Guo, Y. Fan, L. Pan, M. Lang, Y. Jiang, Q. Shao, T. Nie, K. Murata, J. Tang *et al.*, Phys. Rev. Lett. **113**, 137201 (2014).
[7] P. Wei, F. Katmis, B. A. Assaf, H. Steinberg, P. Jarillo-Herrero, D. Heiman, and J. S. Moodera, Phys. Rev. Lett. **110**, 186807 (2013).
[8] M. Lang, M. Montazeri, M. C. Onbasli, X. Kou, Y. Fan, P. Upadhyaya, K. Yao, F. Liu, Y. Jiang, W. Jiang *et al.*, Nano Lett. **14**, 3459 (2014).
[9] F. Katmis, V. Lauter, F. S. Nogueira, B. A. Assaf, M. E. Jamer, P. Wei, B. Satpati, J. W. Freeland, I. Eremin, D. Heiman *et al.*, Nature (London) **533**, 513 (2016).
[10] Y. T. Fanchiang, K. H. M. Chen, C. C. Tseng, C. C. Chen, C. K. Cheng, S. R. Yang, C. N. Wu, S. F. Lee, M. Hong, and J. Kwo, Nat. Commun. **9**, 223 (2018).
[11] R. Watanabe, R. Yoshimi, M. Kawamura, M. Mogi, A. Tsukazaki, X. Z. Yu, K. Nakajima, K. S. Takahashi, M. Kawasaki, and Y. Tokura, Appl. Phys. Lett. **115**, 102403 (2019).
[12] S. R. Yang, Y. T. Fanchiang, C. C. Chen, C. C. Tseng, Y. C. Liu, M. X. Guo, M. Hong, S. F. Lee, and J. Kwo, Phys. Rev. B **100**, 045138 (2019).
[13] S. Bhattacharyya, G. Akhgar, M. Gebert, J. Karel, M. T. Edmonds, and M. S. Fuhrer, Adv. Mater. **33**, 2007795 (2021).
[14] W.-J. Zou, M.-X. Guo, J.-F. Wong, Z.-P. Huang, J.-M. Chia, W.-N. Chen, S.-X. Wang, K.-Y. Lin, L. B. Young, Y.-H. G. Lin *et al.*, ACS Nano **16**, 2369 (2022).
[15] C. Tang, C.-Z. Chang, G. Zhao, Y. Liu, Z. Jiang, C.-X. Liu, M. R. McCartney, D. J. Smith, T. Chen, J. S. Moodera *et al.*, Sci. Adv. **3**, e1700307 (2017).
[16] A. Neubauer, C. Pfleiderer, B. Binz, A. Rosch, R. Ritz, P. G. Niklowitz, and P. Böni, Phys. Rev. Lett. **102**, 186602 (2009).
[17] N. Nagaosa and Y. Tokura, Nat. Nanotechnol. **8**, 899 (2013).
[18] S. Mühlbauer, B. Binz, F. Jonietz, C. Pfleiderer, A. Rosch, A. Neubauer, R. Georgii, and P. Böni, Science **323**, 915 (2009).
[19] X. Z. Yu, N. Kanazawa, Y. Onose, K. Kimoto, W. Z. Zhang, S. Ishiwata, Y. Matsui, and Y. Tokura, Nat. Mater. **10**, 106 (2011).
[20] A. Tonomura, X. Yu, K. Yanagisawa, T. Matsuda, Y. Onose, N. Kanazawa, H. S. Park, and Y. Tokura, Nano Lett. **12**, 1673 (2012).
[21] X. Z. Yu, N. Kanazawa, W. Z. Zhang, T. Nagai, T. Hara, K. Kimoto, Y. Matsui, Y. Onose, and Y. Tokura, Nat. Commun. **3**, 988 (2012).
[22] H. Wu, F. Groß, B. Dai, D. Lujan, S. A. Razavi, P. Zhang, Y. Liu, K. Sobotkiewich, J. Förster, M. Weigand *et al.*, Adv. Mater. **32**, 2003380 (2020).
[23] S. Vélez, S. Ruiz-Gómez, J. Schaab, E. Gradauskaite, M. S. Wörnle, P. Welter, B. J. Jacot, C. L. Degen, M. Trassin, M. Fiebig *et al.*, Nat. Nanotechnol. **17**, 834 (2022).
[24] A. Fert, V. Cros, and J. Sampaio, Nat. Nanotechnol. **8**, 152 (2013).
[25] A. Fert, N. Reyren, and V. Cros, Nat. Rev. Mater. **2**, 17031 (2017).
[26] T. Schulz, R. Ritz, A. Bauer, M. Halder, M. Wagner, C. Franz, C. Pfleiderer, K. Everschor, M. Garst, and A. Rosch, Nat. Phys. **8**, 301 (2012).

[27] X. Zhang, Y. Zhou, K. M. Song, T.-E. Park, J. Xia, M. Ezawa, X. Liu, W. Zhao, G. Zhao, and S. Woo, J. Phys.: Condens. Matter **32**, 143001 (2020).
[28] A. Gerber, Phys. Rev. B **98**, 214440 (2018).
[29] K. M. Fijalkowski, M. Hartl, M. Winnerlein, P. Mandal, S. Schreyeck, K. Brunner, C. Gould, and L. W. Molenkamp, Phys. Rev. X **10**, 011012 (2020).
[30] L. Wang, Q. Feng, H. G. Lee, E. K. Ko, Q. Lu, and T. W. Noh, Nano Lett. **20**, 2468 (2020).
[31] P. Li, J. Ding, S. S.-L. Zhang, J. Kally, T. Pillsbury, O. G. Heinonen, G. Rimal, C. Bi, A. DeMann, S. B. Field *et al.*, Nano Lett. **21**, 84 (2021).
[32] F. Wang, X. Wang, Y.-F. Zhao, D. Xiao, L.-J. Zhou, W. Liu, Z. Zhang, W. Zhao, M. H. W. Chan, N. Samarth *et al.*, Nat. Commun. **12**, 79 (2021).
[33] L. Tai, B. Dai, J. Li, H. Huang, S. K. Chong, K. L. Wong, H. Zhang, P. Zhang, P. Deng, C. Eckberg *et al.*, ACS Nano **16**, 17336 (2022).
[34] G. Kimbell, C. Kim, W. Wu, M. Cuoco, and J. W. A. Robinson, Commun. Mater. **3**, 19 (2022).
[35] M. Algarni, C. Tan, G. Zheng, S. Albarakati, X. Zhu, J. Partridge, Y. Zhu, L. Farrar, M. Tian, J. Zhou *et al.*, Phys. Rev. B **105**, 155407 (2022).
[36] T. Yokouchi, N. Kanazawa, A. Tsukazaki, Y. Kozuka, M. Kawasaki, M. Ichikawa, F. Kagawa, and Y. Tokura, Phys. Rev. B **89**, 064416 (2014).
[37] X. Zhang, S. C. Ambhire, Q. Lu, W. Niu, J. Cook, J. S. Jiang, D. Hong, L. Alahmed, L. He, R. Zhang *et al.*, ACS Nano **15**, 15710 (2021).
[38] J. H. Jeon, H. R. Na, H. Kim, S. Lee, S. Song, J. Kim, S. Park, J. Kim, H. Noh, G. Kim *et al.*, ACS Nano **16**, 8974 (2022).
[39] K. Yasuda, R. Wakatsuki, T. Morimoto, R. Yoshimi, A. Tsukazaki, K. S. Takahashi, M. Ezawa, M. Kawasaki, N. Nagaosa, and Y. Tokura, Nat. Phys. **12**, 555 (2016).
[40] C. Liu, Y. Zang, W. Ruan, Y. Gong, K. He, X. Ma, Q.-K. Xue, and Y. Wang, Phys. Rev. Lett. **119**, 176809 (2017).
[41] Q. L. He, G. Yin, A. J. Grutter, L. Pan, X. Che, G. Yu, D. A. Gilbert, S. M. Disseler, Y. Liu, P. Shafer *et al.*, Nat. Commun. **9**, 2767 (2018).
[42] J. Chen, L. Wang, M. Zhang, L. Zhou, R. Zhang, L. Jin, X. Wang, H. Qin, Y. Qiu, J. Mei *et al.*, Nano Lett. **19**, 6144 (2019).
[43] J. Jiang, D. Xiao, F. Wang, J.-H. Shin, D. Andreoli, J. Zhang, R. Xiao, Y.-F. Zhao, M. Kayyalha, L. Zhang *et al.*, Nat. Mater. **19**, 732 (2020).
[44] R. Xiao, D. Xiao, J. Jiang, J.-H. Shin, F. Wang, Y.-F. Zhao, R.-X. Zhang, A. Richardella, K. Wang, M. Kayyalha *et al.*, Phys. Rev. Res. **3**, L032004 (2021).
[45] M. X. Guo, C. K. Cheng, Y. C. Liu, C. N. Wu, W. N. Chen, T. Y. Chen, C. T. Wu, C. H. Hsu, S. Q. Zhou, C. F. Chang *et al.*, Phys. Rev. Mater. **6**, 054412 (2022).
[46] K. Y. Lin, H. W. Wan, K. H. M. Chen, Y. T. Fanchiang, W. S. Chen, Y. H. Lin, Y. T. Cheng, C. C. Chen, H. Y. Lin, L. B. Young *et al.*, J. Cryst. Growth **512**, 223 (2019).
[47] M. Hong, M. Passlack, J. P. Mannaerts, J. Kwo, S. N. G. Chu, N. Moriya, S. Y. Hou, and V. J. Fratello, J. Vac. Sci. Technol. B **14**, 2297 (1996).
[48] M. Hong, J. Kwo, A. R. Kortan, J. P. Mannaerts, and A. M. Sergent, Science **283**, 1897 (1999).
[49] J. Kwo, M. Hong, A. R. Kortan, K. T. Queeney, Y. J. Chabal, J. P. Mannaerts, T. Boone, J. J. Krajewski, A. M. Sergent, and J. M. Rosamilia, Appl. Phys. Lett. **77**, 130 (2000).
[50] M. Hong, J. Kwo, S. N. G. Chu, J. P. Mannaerts, A. R. Kortan, H. M. Ng, A. Y. Cho, K. A. Anselm, C. M. Lee, and J. I. Chyi, J. Vac. Sci. Technol. B **20**, 1274 (2002).
[51] Y. H. G. Lin, H. W. Wan, L. B. Young, J. Liu, Y. T. Cheng, K. Y. Lin, Y. J. Hong, C. T. Wu, J. Kwo, and M. Hong, Appl. Phys. Lett. **118**, 252104 (2021).
[52] P. Dutta, A. Pariari, and P. Mandal, Sci. Rep. **7**, 4883 (2017).
[53] L.-X. Qin, X.-C. Pan, F.-Q. Song, L. Zhang, Z.-H. Sun, M.-Q. Li, P. Gao, B.-C. Lin, S.-M. Huang, R. Zhu *et al.*, Appl. Phys. Lett. **112**, 032102 (2018).
[54] P. A. Lee and T. V. Ramakrishnan, Rev. Mod. Phys. **57**, 287 (1985).
[55] J. Wang, A. M. DaSilva, C.-Z. Chang, K. He, J. K. Jain, N. Samarth, X.-C. Ma, Q.-K. Xue, and M. H. W. Chan, Phys. Rev. B **83**, 245438 (2011).
[56] P. Li, J. Kally, S. S.-L. Zhang, T. Pillsbury, J. Ding, G. Csaba, J. Ding, J. S. Jiang, Y. Liu, R. Sinclair *et al.*, Sci. Adv. **5**, eaaw3415 (2019).
[57] See Supplemental Material at http://link.aps.org/supplemental/10.1103/PhysRevB.109.024432 for data processing using the antisymmetrization method, Hall measurements using the minor loop method, discussion on the possibility of Hall effect data from nonlinear OHE background or two distinct AHE contributions, the rationale of a square hysteresis for the AHE loop to derive THE, table for the comparison of THE in various systems hosting magnetic skyrmions, temperature- and gate-dependent THE loops, estimate of manipulated by gate bias, gate-dependent results of one additional field-effect device, and clarification to accentuate the differences between this work and the previous gate-dependent THE results, which includes Refs. [12,14,16,28–34,36,37,39,41,42,45,58–60,66–68,70–80].
[58] N. Bansal, Y. S. Kim, M. Brahlek, E. Edrey, and S. Oh, Phys. Rev. Lett. **109**, 116804 (2012).
[59] A. A. Taskin, S. Sasaki, K. Segawa, and Y. Ando, Phys. Rev. Lett. **109**, 066803 (2012).
[60] F. Yang, A. A. Taskin, S. Sasaki, K. Segawa, Y. Ohno, K. Matsumoto, and Y. Ando, Appl. Phys. Lett. **104**, 161614 (2014).
[61] J. Matsuno, N. Ogawa, K. Yasuda, F. Kagawa, W. Koshibae, N. Nagaosa, Y. Tokura, and M. Kawasaki, Sci. Adv. **2**, e1600304 (2016).
[62] S. X. Huang and C. L. Chien, Phys. Rev. Lett. **108**, 267201 (2012).
[63] J. C. Gallagher, K. Y. Meng, J. T. Brangham, H. L. Wang, B. D. Esser, D. W. McComb, and F. Y. Yang, Phys. Rev. Lett. **118**, 027201 (2017).
[64] S. A. Meynell, M. N. Wilson, J. C. Loudon, A. Spitzig, F. N. Rybakov, M. B. Johnson, and T. L. Monchesky, Phys. Rev. B **90**, 224419 (2014).
[65] M. Leroux, M. J. Stolt, S. Jin, D. V. Pete, R. C., and B. Maiorov, Sci. Rep. **8**, 15510 (2018).
[66] Q. Shao, Y. Liu, G. Yu, S. K. Kim, X. Che, C. Tang, Q. L. He, Y. Tserkovnyak, J. Shi, and K. L. Wang, Nat. Electron. **2**, 182 (2019).
[67] Y. Ohuchi, Y. Kozuka, M. Uchida, K. Ueno, A. Tsukazaki, and M. Kawasaki, Phys. Rev. B **91**, 245115 (2015).
[68] B. Sohn, B. Kim, S. Y. Park, H. Y. Choi, J. Y. Moon, T. Choi, Y. J. Choi, H. Zhou, J. W. Choi, A. Bombardi *et al.*, Phys. Rev. Res. **3**, 023232 (2021).

[69] J. S. Lee, A. Richardella, D. R. Hickey, K. A. Mkhoyan, and N. Samarth, Phys. Rev. B **92**, 155312 (2015).
[70] Y. Ohuchi, J. Matsuno, N. Ogawa, Y. Kozuka, M. Uchida, Y. Tokura, and M. Kawasaki, Nat. Commun. **9**, 213 (2018).
[71] Y. Deng, Y. Yu, M. Z. Shi, Z. Guo, Z. Xu, J. Wang, X. H. Chen, and Y. Zhang, Science **367**, 895 (2020).
[72] A. Gao, Y.-F. Liu, C. Hu, J.-X. Qiu, C. Tzschaschel, B. Ghosh, S.-C. Ho, D. Bérubé, R. Chen, H. Sun *et al.*, Nature (London) **595**, 521 (2021).
[73] Y.-F. Zhao, L.-J. Zhou, F. Wang, G. Wang, T. Song, D. Ovchinnikov, H. Yi, R. Mei, K. Wang, M. H. W. Chan *et al.*, Nano Lett. **21**, 7691 (2021).
[74] H. Peng, K. Lai, D. Kong, S. Meister, Y. Chen, X.-L. Qi, S.-C. Zhang, Z.-X. Shen, and Y. Cui, Nat. Mater. **9**, 225 (2010).
[75] J. Chen, H. J. Qin, F. Yang, J. Liu, T. Guan, F. M. Qu, G. H. Zhang, J. R. Shi, X. C. Xie, C. L. Yang *et al.*, Phys. Rev. Lett. **105**, 176602 (2010).
[76] H.-T. He, G. Wang, T. Zhang, I.-K. Sou, G. K. L. Wong, J.-N. Wang, H.-Z. Lu, S.-Q. Shen, and F.-C. Zhang, Phys. Rev. Lett. **106**, 166805 (2011).
[77] S. Hikami, A. I. Larkin, and Y. Nagaoka, Prog. Theor. Phys. **63**, 707 (1980).
[78] Z. Jiang, F. Katmis, C. Tang, P. Wei, J. S. Moodera, and J. Shi, Appl. Phys. Lett. **104**, 222409 (2014).
[79] J. J. Cha, D. Kong, S.-S. Hong, J. G. Analytis, K. Lai, and Y. Cui, Nano Lett. **12**, 1107 (2012).
[80] J. Zhang, C.-Z. Chang, Z. Zhang, J. Wen, X. Feng, K. Li, M. Liu, K. He, L. Wang, X. Chen *et al.*, Nat. Commun. **2**, 574 (2011).